LM-02K005
February 27, 2002

Effect of Corrosion Film Composition and Structure on the Corrosion Kinetics of Ni-Cr-Fe Alloys in High Temperature Water

P.M. Rosecrans, N. Lewis, D.J. Duquette

NOTICE

024005

Effect of Corrosion Film Composition and Structure on the Corrosion Kinetics of Ni-Cr-Fe Alloys in High Temperature Water

PM Rosecrans, N Lewis and DJ Duquette

Abstract

Nickel alloys such as Alloy 600 undergo Stress Corrosion Cracking (SCC) in pure water at temperatures between about 260° C and the critical point. Increasing the level of Cr in Ni-Fe-Cr alloys increases SCC resistance in aerated and deaerated water. The mechanism is not understood. The effect of Cr composition on oxide microstructure and corrosion kinetics of Ni-Fe-Cr alloys was determined experimentally, to evaluate whether the anodic dissolution model for SCC can account for the effect of Cr on SCC. The alloy corrosion rate and corrosion product oxide microstructure is strongly influenced by the Cr composition. Corrosion kinetics are parabolic and influenced by chromium concentration, with the parabolic constant first increasing then decreasing as Cr increases from 5 to 39%. Surface analyses using Analytical Electron Microscopy (AEM) and Auger Electron Spectroscopy (AES) show that the corrosion product film that forms initially on all alloys exposed to high purity high temperature water is a nickel rich oxide. With time, the amount of chromium in the oxide film increases and corrosion proceeds toward the formation of the more thermodynamically stable spinel or hexagonal Cr-rich oxides, similar to high temperature gaseous oxidation. Due to the slower diffusion kinetics at the temperatures of water corrosion compared to those in high temperature gaseous oxidation, however, the films remain as a mixture of NiO, mixed Ni, Fe and Cr spinels, $NiCrO_3$ and $FeCrO_3$. As the amount of Cr in the film increases and the nature of the film changes from NiO to spinel or hexagonal oxides, cation diffusion through the films slows, slowing the corrosion rate. These observations are qualitatively consistent with an anodic dissolution SCC mechanism. However, parametric modeling of the SCC growth process, applying available creep, oxide rupture strain and corrosion kinetics data, indicates that the anodic dissolution mechanism accounts for only a fraction of the effect of Cr on SCC resistance

Introduction

There has been considerable work to characterize the stress corrosion cracking of austenitic materials in nuclear plant service. Intergranular SCC of austenitic stainless steel alone has cost over a billion dollars in research, repair and mitigation (1). In systems where Ni-Cr-Fe alloys are used, the higher Cr content Alloy 690 has largely replaced Alloy 600 as the material of

choice in SCC-prone applications (2-4). The fundamental reason why Cr has a beneficial effect on pure, high temperature water SCC resistance is not well understood.

There is not a universally accepted SCC mechanism for Ni alloys in high temperature water. There are two classes into which most mechanistic descriptions fall: anodic dissolution (5-7) and hydrogen assisted cracking (8-10). The two processes are closely linked and experimental separation is difficult, e.g., conditions, which decrease crack tip corrosion rate also, reduce the hydrogen generation rate. Sub-processes that are influenced by Cr content, such as creep rate, corrosion rate and oxide film mechanical properties, are common to both anodic dissolution and hydrogen assisted cracking mechanisms.

The Ford-Andresen description (7,11-12) has been used to describe SCC of stainless steel in BWR environments. The concept is that structural damage of the oxide film at the crack tip results in rapid local corrosion of the underlying metal. This corrosion repairs the oxide, slowing down the corrosion rate until the film is again damaged. Qualitative descriptions of this model refer to slip emergence at the crack tip as the damage mechanism. Quantitatively,

$$V_{scc} = \frac{M}{\rho Z F} \frac{i_o t_o^n}{1-n} \left(\frac{\dot{\varepsilon}_c}{\varepsilon_f} \right)^n \qquad \text{Eqn (1)}$$

where,

V_{scc}- average crack tip extension rate

Z - number of electrons

F - Faraday's constant

$i_o, t_{o,n}$ - from repassivation profile

ε_f - oxide rupture strain

$\dot{\varepsilon}_c$ -crack tip strain rate

M - atomic weight

ρ = metal density

In practical application, the individual material properties such as creep rate and oxide rupture strain have not been determined explicitly. SCC growth rates in stainless steel are predicted through empirical correlations between the stress state and the crack tip strain rate and with values taken from a repassivation current decay curve. Subsequent work by other

researchers has shown the same analytical approach is consistent with the SCC behavior of Alloy 600 (13,14).

The three key material properties associated with the anodic dissolution mechanism are also important for any hydrogen-assisted mechanism, i.e. creep, oxide rupture strain and corrosion kinetics. Of the three, more data are available on creep for the Ni-Cr-Fe alloy system. This work provides data on the formation kinetics of Ni-Cr-Fe corrosion films as a function of Cr content. In addition, oxide film characterization is presented to understand how Cr content influences corrosion kinetics in high temperature water. This data, when combined with the available information on creep and oxide mechanical properties (15), provides insight on how Cr content influences SCC.

Experimental

Nickel base alloys with Cr contents of 5, 16, 23, 30 and 39% (weight) were machined into test specimens and exposed to high temperature water to form oxide films appropriate for measuring corrosion kinetics and for microcharacterization.

Materials

The materials used in this study were from commercially available and laboratory fabricated alloys. Five laboratory-fabricated alloys were tested so that only Cr and Ni concentrations were varied. The remaining minor alloy element concentrations were held constant and representative of Alloy 600 components produced for nuclear plant service (16, 17). Since commercial alloys have slightly different target carbon levels, a laboratory version of Alloy 690 was made with a carbon level characteristic of commercial Alloy 600. Samples from commercially produced heats of Alloy 600 and Alloy 690 were taken from 7.6 cm diameter bars fabricated by Teledyne Allvac and International Nickel-Huntington Alloys. Information on the chemical composition and other properties of these materials is presented in Table 1.

Ingots were fabricated using a double vacuum arc melting process. After a 1-hour homogenization, the ingots were reduced to a nominal thickness of 1 cm by hot rolling on a two roll, 20 cm diameter rolling mill. Homogenization temperatures, tabulated below, were selected to produce materials that were as metallurgically equivalent as possible, in terms of second phase particle distribution. Metallography was used to confirm that the processing resulted in a final product with a uniform, intragranular distribution of carbide particles.

Alloy	Homogenization and Final Anneal Temperature (°C)
5% Cr	1050
23% Cr	1150
30% Cr	1200
39% Cr	1250

Test Methods

Flat coupon specimens, 81x13x3 mm, were fabricated from each material. The specimens were prepared by machining from the rolled plates using a combination of electric discharge machining for initial specimen removal, conventional milling and a final grinding pass to produce a surface with a 8 micron surface finish. To facilitate characterization, one side of each sample was further polished through 0.05 micron alumina powder. These coupons were then cleaned with mild detergent and isopropanol and hung with a Ni wire on a stainless steel rack assembly which was placed in the autoclave. All autoclaves were made from austentitic stainless steel. Weight gains were monitored by comparing the initial and final coupon weights measured on a Mettler balance with a sensitivity of 10^{-5} g. Samples were exposed to water buffered to a room temperature pH of 10.2, with a hydrogen concentration of 40 scc/kg. Coupons were exposed for 64-120 days at temperatures of 288, 316, 338 and 360° C.

Oxide surfaces were evaluated by Auger Electron Spectroscopy (AES) to determine how oxide chemistry changed with chromium content. Composition depth profiles were generated by argon sputtering. The sputtering rate, calibrated to a flat SiO_2/Si standard, was 0.3 nm/s. In addition, selected samples were analyzed by using a Analytical Electron Microscope (AEM). Samples were sectioned, leaving the oxide surface intact and thinning from the cut metal side only. Samples for AEM were then thinned by mechanical grinding on SiC paper to a thickness of about 75 microns, mechanical dimpling using 3 micron diamond paste and electropolishing with 20% perchloric acid in methanol. The thinned samples were evaluated in a Phillips EM420 analytical electron microscope. Selected area electron diffraction and convergent beam diffraction were performed to assist in phase identification. X-ray spectroscopy was used to determine the elemental distributions within the oxides. An Alloy 600 specimen exposed for a longer time than the other samples (1095 days at 288° C) was also characterized, to provide more insight into time dependent oxide structure changes.

Results

Corrosion Kinetics

The visual appearance of the films was markedly different as a result of thickness variations, with no film evident visually at 288° C on the alloy with 5% Cr. In addition, the films were not completely tenacious as the film thickness increased. For example, firm rubbing with a cotton cloth was sufficient to remove the outermost film. The lack of complete adherence is confirmed by gravimetric results. After about 90 days of exposure, weight losses are evident for most coupons. Based on these observations, along with the low level of expected oxide film solubility in this environment (18), the weight loss is attributed to handling.

A representative corrosion kinetics plot is shown in Figure 1, in the form of weight gain as a function of time. A linear regression analysis was carried out on each data set, and a parabolic equation of the form:

$$W=k_p t^{1/2} \qquad \text{Eqn (2)}$$

where, W-weight gain

k_p-parabolic constant

t-exposure time

gave the best overall fit for the data. This implies that the corrosion process follows Wagner's model for diffusion controlled kinetics (19). Values of the parabolic coefficients k_p is presented as a function of temperature and Cr composition in Figures 2 and 3.

Oxide Film Microstructure

Results from twelve samples characterized by AEM are summarized in Table 2 and representative AEM results are presented in Figures 4-7. Figures 4 and 5 represent oxides formed on an alloy with 23% Cr, after 5 and 64 days exposure, respectively. The film formed after five days at 288° C exhibited a continuous grain size variation from 5 to 100 nm, with the finest grains nearest to the metal-oxide interface and the largest grains in contact with the environment. This grain size variation was observed in all of the samples characterized. Fig. 4 illustrates the continuum nature of the crystal size distribution. Electron diffraction patterns on this sample

reveal the NiO cubic structure. Wide local variation in Cr content is observed throughout the film thickness. Nevertheless, even in regions of high Cr content, no evidence of hexagonal Cr_2O_3 was observed. It can be speculated that the high Cr regions are amorphous or have a similar spacing to NiO. However, no other phase could be indexed. The film shown in Figure 5, formed after 64 days at 360° C, exhibits the same oxide grain size variation. Oxide grains near the metal interface are very fine (5-10 nm), with larger outer grains measuring 50-150 nm. Chemical analysis showed that the fine grains are enriched in Cr relative to Fe and Ni. The large outer grains were iron and nickel rich and were identified using electron diffraction as nickel ferrite grains having a spinel structure.

A film formed on the 39% Cr alloy, after exposure to 360° C water for 64 days, is shown in Figure 6. Again, a grain size variation throughout the oxide layer thickness is observed. Fine grains observed near the metal substrate interface are 10-20 nm in size. These grains are enriched in Cr relative to the base metal. The largest oxide grains (up to 1500 nm) on the outermost surface contained Ni and Fe and indexed to a spinel $NiFe_2O_4$. The remainder of the film also has a spinel structure with some evidence of a hexagonal phase present. The continuous variation in grain size from the metal interface to the outermost surface is clearly evident.

To provide more insight into the film maturation process, a long-term exposure sample (16% Cr; 1095 days in 288°C water) was evaluated. The same grain size variation observed for the other samples were also seen here, with outer film grains about 100-200 nm in diameter and inner film grains about 10-20 nm. In this case, the outer film shows a spinel diffraction pattern, while the inner film shows a mixture of hexagonal and spinel phases. Local chemistry variation is again evident, with the coarsest outer grains being lowest in Cr and highest in Fe. Oxide closer to the metal surface is higher in Cr. Images are presented in Figure 7.

Key observations from the AEM work are:

1. The film forming initially on all alloys upon exposure to high purity high temperature water is nickel rich oxide.

2. As exposure time increases, the amount of chromium in the oxide film increases. This is manifested as both higher Cr levels within the cubic NiO structure and in the form of spinel or hexagonal phases commonly associated with chrome-rich oxides.

3. The gradual incorporation of chromium within the film takes place in a heterogeneous manner across the film.

4. The oxides have a microstructure that is finest at the metal oxide interface and becomes coarser toward the oxide-environment interface, with a corresponding change in chemistry.

5. Fine oxide grains are seen at the metal oxide interface, and are enriched in Cr relative to the base metal. Coarse outer grains contain predominantly Fe and Ni cations.

Representative AES results are shown in Figures 8-10. Composition profiles are presented in terms of sputtering time, which is proportional to distance below the oxide surface. Key observations from these samples are:

1. Chromium concentration in the oxides generally decreased more abruptly from the metal-oxide interface to the oxide-environment interface than Fe concentration.

2. Spatial differences in Cr composition were evident. For Alloy 690 samples, for example, some regions (20 nm diameter) selected for sputtering exhibited films high in chromium while other regions were devoid of chromium. This first became evident when it became difficult to reproduce the initial result on a 39% Cr sample showing high Cr levels within the film unless multiple areas were scanned. Scanning electron microscopy on the coupons revealed that this variability correlates with base metal crystallography. The oxide film over some base metal grains is thicker and topographically rougher than over other grains.

3. For alloys with chromium content $\leq$ 23%, the oxide films contained less Cr than Ni, and a higher Ni/Cr ratio, than in the bulk alloy. For the higher Cr alloys, regions existed where Cr concentration in the film exceeds the Ni concentration.

Discussion

Film Formation: Microstructure

The oxide characterization results help to elucidate the corrosion product formation process on NiFeCr alloys and create a conceptual framework for how the oxides form and change with time. From the summary in Table 2 it is clear that oxides formed by short time (a few days) exposure to high temperature water are predominantly nickel oxide. As exposure time increases, higher levels of Cr are seen in the oxide, and the oxide crystal structure shows evidence of the Cr-rich phases such as spinels and some hexagonal (chromia-type) structures. The AEM work shows a finer grain structure, richer in Cr, at the metal-oxide interface than at points approaching the oxide-environment interface. The oxide structure is shown schematically in Figure 11.

For corrosion in high temperature water in alloys with <16% Cr, Ni is the predominant species and makes up most of the initial oxide. Although Cr oxidizes readily, it takes time at temperature to form a continuous Cr rich oxide layer. During this time, the faster and more highly soluble Fe and Ni diffuse toward the outer portion of the film.

Alloys with 16-39% Cr form a continuous Cr rich oxide more readily than alloys with less Cr, since less diffusion is required. The films mature with time (transient oxidation) from NiO to compounds, which are more thermodynamically stable. Typically, Cr rich spinels and sometimes Cr_2O_3 type oxides are observed near the metal oxide interface, and spinels ($NiFe_2O_4$) near the oxide environment interface after 60 days of exposure. Although NiO forms initially, chromium-bearing oxides form more slowly and occupy the metal oxide interfacial region. Iron bearing oxides dominate the oxide environment region, due to faster diffusion of Fe. Possibly, in part, the coarsest outer oxides form as a result of reprecipitation from solution. Areas of the alloy which are locally Cr-enriched, such as over a carbide particle or network, would be expected to undergo the transition from NiO to a mixed oxide sooner than other areas. Since corrosion of austenitic alloys is likely to be cation diffusion limited (19, 20), and diffusion is slower through the Cr-rich spinel and hexagonal oxides, general corrosion rates will be influenced.

Information from Prior Related Studies

These results are consistent with previous studies on closely related metal-environment systems such as films on Ni alloys formed in water or gaseous environments and films on austenitic stainless steels formed in water (References 20-23). There are no prior systematic studies of how Cr influences the rate of oxide formation in water for NiFeCr alloys, but results from closely related systems is consistent with the observations made here. While most previous studies of oxide films on NiFeCr alloys were done on thicker films formed at higher temperatures, review of that work indicates that a film growth model in which an initial NiO film gradually transforms to a film with significant concentrations of Cr rich phases is common, as described below.

Studies of the nature of oxide film formation in Fe-Cr and Ni-Cr films in pure oxygen at 600° C are of particular interest to the problem at hand. Although the oxides are formed much faster than in the high temperature water experiments conducted here, the thickness of the oxide formed in 1-15 minutes at 600° C is comparable to films formed over a period of months or years in high temperature water. Chattopadhyay and Wood (20) studied the nature of films formed after very short exposures in pure oxygen, using binary Fe+Cr or Ni+Cr alloys with nominal compositions of 5,10,15 and 30w/o Cr. The first oxide to form on all of the Ni alloys was NiO. It was observed that for dilute alloys (<10% Cr), the amount of $NiCr_2O_4$ spinel increased with time, and existed primarily as particles produced between the main NiO layer and a Cr_2O_3 oxide. As Cr increased in the alloy, the amount of Cr_2O_3 detected was increased and was detectable at earlier exposure times. In addition, oxide formed over metal grain boundaries, subgrain boundaries or other defect features was thicker than elsewhere. The authors hypothesized that these areas serve as vacancy sinks or provide short circuit diffusion paths, or both. Finally, it was observed that as the Cr alloy content increased, it became easier or more likely that Cr-rich oxides would be observed at the metal-oxide interface, creating an oxide which would grow more slowly. For the dilute Ni-Cr alloys, development of this slowly growing Cr-rich oxide began by nucleation above metal grain boundaries. The slow growing Cr-rich oxide developed more quickly for the 15% Cr alloy than for more dilute alloys, although with substantial local area-to-area variability. For the 30% Cr alloy, development of the Cr-rich oxide occurred even more quickly.

It is reasonable to draw an analogy between the oxidation mechanism of this binary alloy system in the early stages (<200 nm) in 600° C oxygen and the formation of such a film on the alloys of interest in water at 280-360° C in a similar thickness range. The Chattopadhyay and Wood (20) work implies that a maturation cycle occurs for the oxide, in which the initial NiO film gradually transforms to a more thermodynamically stable form with time. For example:

1. A uniform general corrosion product film of NiO forms initially.

2. Cr-rich zones form at the metal oxide interface. The oxidation rate slows locally in these zones.

3. The Cr-rich zones interact with the NiO to create particles of $NiCr_2O_4$.

Gaseous oxidation of Alloy 600 was studied over the 100-700° C range, and similar but more limited work was reported in (22). Key observations from this work include the following:

1. Initially, oxides of Ni, Fe and Cr form in proportion to their concentration in the base metal.

2. At temperatures of 280° C and below, which is similar to the exposure temperatures in the current investigation, Ni oxide grows and becomes dominant, due to the slower diffusion of Cr in the oxide, even though Cr_2O_3 is more stable thermodynamically.

3. Even at temperatures as low as 100-280° C, the individual metal oxides of Ni, Fe and Cr have at least partially reacted locally to form nickel chromites and ferrites.

4. A layered structure, with the more Cr-rich phase (either chromia or one of the ternary oxides) close to the metal oxide interface, is observed above 280° C. The work herein indicates that the duplex structure discussed in Refs. 21-23 may be more accurately described as film with a grain size variation that changes rapidly throughout the oxide layer thickness.

5. At 500-700° C, chromium diffusion is sufficiently rapid that Cr-rich phases dominate.

The maturation process implied in this paper was also described for the Ni-Cr system based on observations from gaseous oxidation (29). There, a film structure consisting of NiO at the oxide-environment interface and mixtures of NiO, $NiCr_2O_4$ and Cr_2O_3 closer to the metal-environment interface was observed. A three step mechanism was described. Rapid local oxidation of Cr to form Cr_2O_3 occurs first. This is followed by the growth of NiO past and surrounding the chromia zone. Finally, two oxides react to form nickel chromite. The higher Cr oxides are reported to slow Ni^{+2} cation diffusion, slowing the oxidation rate. The time, during which the mixed oxides exist, referred to as a transient oxidation period, is reduced as the Cr content of the

alloy is increased. Above a critical level of chromium, reported to be about 12 atomic percent at 1000° C, a dramatic reduction in the oxidation rate is observed.

These previous results from closely related metal-environment systems are similar in several ways to the systematic study conducted here. In both gaseous oxygen and water, NiO forms as the initially predominant phase. A maturation process occurs within the oxides formed in both environments. The system evolves over time toward a Cr_2O_3 structure, since that is the most stable oxide. In the films characterized in this study, there was some evidence of Cr_2O_3 and considerable evidence both of the $NiCr_2O_4$-type oxides and of localized increased Cr concentration in the film close to the metal-oxide interface. The maturation cycle involving NiO evolving to spinels or Cr_2O_3 is evident from experimental observations in all of the studies.

Film Formation: Kinetics

General corrosion kinetics were measured to better understand the events that occur immediately after breaching the oxide film during stress corrosion cracking. Short time measurements of the repassivation transient have been made in the past and have provided some insight (13, 24). There has been little reported gravimetric characterization, even though gravimetric and repassivation methods give complementary information. Repassivation measurements are experimentally more complex, and produce data for a period of seconds or minutes. Gravimetric measurements require long exposure times for meaningful data, and lose accuracy if the film is not completely tenacious, if tenacious environmental precipitates exist or if the film has appreciable solubility in the environment. However, data for exposure times much longer than a few minutes can be obtained. The gravimetric measurements performed here are intended to supplement the existing work done with repassivation transients and the gravimetric data that exists in the historical literature.

Kinetics studies were previously reported for water exposure (25, 26). Tests involving gaseous exposure are more common. The common theme in prior studies is the observation that kinetics is well described as a parabolic (equation 2). The pre-exponential factor, k_p, has been noted in some studies to be a function of the oxide film properties, particularly composition and grain size. Studies in high temperature water have been more extensive on stainless steel, with the common observation (27) that k_p is greater for magnetite films than for spinels, and is lower still for M_2O_3 type films. The difference has been attributed to the relationship between k_p and

the diffusion coefficient. Since the diffusion coefficient through these oxides varies in the manner:

$$Fe^{+2} > Ni^{+2} >> Cr^{+3}$$

The higher Cr bearing spinels and hexagonal oxides will inherently reduce the rate of cation transport necessary for their growth.

Key observations from the kinetics data in this study are:

1. Corrosion kinetics are well described by the parabolic equation.

2. Oxide films are not completely tenacious. Some weight loss is seen for most samples between 64-120 days of exposure in these environments.

3. Corrosion rate increases with temperature. The temperature sensitivity of corrosion, as described by the estimated activation energy for the process, is about 14 kJ/m (3.3 kcal/m) for Alloy 690 and 37.3 kJ/m (18.4 kcal/m) for Alloy 600.

4. The corrosion rate is a function of the chromium concentration in the alloy (Figures 2 and 3).

For materials with 16% Cr or more k_p decreases with increasing Cr content above 335° C. The 5% Cr alloy does not fit this trend, and is in fact harder to characterize gravimetrically. At 360° C this alloy showed a gradual weight loss after initial exposure, indicating that the film is not tenacious. However, the observation that k_p first increases and then decreases with Cr content in nickel alloys is consistent with previous work associated with high temperature gaseous oxidation. Giggins and Petit report on work in which k_p increases with chromium content in the binary Ni-Cr system between 0 and 3% Cr, but decreases again at 10% Cr (28). This can be explained by the competing effects associated with increasing Cr content. Increasing cation vacancy concentration tends to increase diffusion while increasing the amount of Cr-rich oxide phases at the metal oxide interface tends to slow diffusion.

The corrosion kinetics work presented here can be used to provide insight into the effect of Cr on SCC. From the kinetics experiments, it is clear that increasing Cr content above the 16% level decreases both corrosion rate and temperature sensitivity. If an anodic dissolution mechanism is operative, this would account for part of the improved SCC performance of the high Cr materials. If a hydrogen mechanism is operative, the slower corrosion kinetics would decrease the amount of monatomic hydrogen available from the corrosion reaction, also helping to account in part for the improved SCC resistance of the higher Cr material.

Of course, corrosion rate is only one of the three key material property variables that is influenced by Cr content. Low temperature aqueous creep strength is increased significantly by increasing Cr content (30-34), and oxide rupture strain increases with Cr content (15). To assess whether the effect of Cr can be explained by the influence Cr exerts on one of these material properties, the anodic dissolution framework will be used to analyze the available experimental information. Such an analysis can identify shortcomings in how well an anodic dissolution model describes the effect of Cr on the SCC process and therefore point toward strategies for model refinement.

Creep

The influence of Cr on base metal creep has been characterized for both laboratory-processed and commercial materials (30-34). The conditions of interest, increasing Cr content from 16 to 30% in the alloy decreased the creep rate by a factor of 3-8. The following expression was developed for the average creep behavior of the 16 and 30% Cr alloys:

$$\dot{\varepsilon}_c = K_{16,30}\left(\frac{\sigma - \sigma_y}{\sigma_1}\right)^{0.86} e^{\frac{-180,000}{RT}} t^{-0.47} \qquad \text{Eqn (3)}$$

where, $K_{16,30}$ -constant for the 16 and 30% Cr alloys, respectively

K_{16} - 2.38×10^{10} ; K_{30} - 1.30×10^{10} $hr^{-0.53}$

σ - stress

σ_y - yield strength

t - time T- absolute temperature

$\dot{\varepsilon}_c$ - creep strain rate

R -Universal Gas Constant (8.31 J/mol K)

This prior work demonstrated that dislocation controlled creep is the predominant mechanism in the alloy system of interest, and that creep is a function of both the C and Cr level in the material. The effect of Cr has been attributed principally to solid solution strengthening. Base metal creep occurs above the yield stress, so some additional creep resistance can be expected for higher Cr alloys on the basis of increased yield strength. At a given ratio of applied stress to yield strength, the amount of creep strain accumulated in a given time is about 83% greater for the 16% alloy than for the 30% alloy.

Oxide Rupture Strain

As reported in (15) oxide rupture strain increases by 50% as the base metal Cr content increases from 16 to 30%. In the absence of other differences, Eqn. 1 would predict a 50% decrease in crack growth rate for Alloy 690 when compared with Alloy 600. However, the wide variety of SCC tests conducted over the past two decades has demonstrated that the difference in primary water SCC resistance of Alloy 690 is far more than a factor of two; in fact cases of observable SCC growth in Alloy 690 in primary water environments are rare (35). Unless the difference can be attributed to initiation effects, the effect of Cr on oxide rupture strain as reflected in Eqn. 1 is insufficient to account for the SCC differences between Alloys 600 and 690.

Corrosion Kinetics

Equation 1 makes use of short-term repassivation test data to quantify SCC growth rates. As noted previously, such test results cover a time period of seconds to minutes. Corrosion kinetics data representative of longer exposure times may be more appropriate for the SCC of NiFeCr alloys in water. The time period over which corrosion kinetics control the rate of SCC with an anodic dissolution mechanism is greater than a few minutes under conditions of practical interest. For example, considering Alloy 600 at 360° C, and applying the creep and oxide rupture strain data presented previously, the time between oxide rupture events can be estimated as:

$$t_r = \frac{\varepsilon_f}{\dot{\varepsilon}_c} = 0013/\dot{\varepsilon}_c \qquad \text{Eqn. (4)}$$

Values of $\dot{\varepsilon}_c$ are a function of stress state and time, and therefore are highly dependent on the specific test specimen or component and on environmental conditions. Taking the case of a standard constant displacement test specimen such a the U-Bend specimens tested in this study, and assuming a specimen is loaded to 2.5 times yield strength, the average strain rate due to creep relaxation after the first day of exposure would be on the order of 2×10^{-5} hr^{-1}, based on Eqn. 3. This equates to an estimated time between oxide rupture events of:

$$t_r = \frac{\varepsilon_f}{\dot{\varepsilon}_c} = .0013/2 \times 10^{-5} = 65 \text{ hours} \qquad \text{Eqn. (5)}$$

A similar calculation based on the creep rate after 30 days would give a time between events of about 1 week. Certainly more aggressive loading conditions could decrease the

estimated times, but these estimates are representative of many examples of practical test specimens and applications. The estimates demonstrate that the longer time gravimetric data are appropriate for this alloy - environment system.

To make use of the gravimetric data, the mathematics of the film-rupture model can be reformulated. The corrosion kinetics for the materials of interest can be described by equations of the form $W=k_p t^{1/2}$ for each alloy system. The linear constant k_p varies for each alloy, consistent with the theoretical work of Wagner (19), the gravimetric data obtained here, and gravimetric data obtained in gaseous oxidation studies (20, 28). If these equations represent the corrosion kinetics from the start of the corrosion process, a slightly different formulation than the power law relationship used to develop Eqn. 1 would apply.

Assuming that the corrosion rate can be described by an equation of the Wagner form: $W=k_p t^{1/2}$, the total charge transferred in a given time is described by:

$$Q = \frac{ZF}{M} k_p t^{1/2} \qquad \text{Eqn (6)}$$

Observable SCC growth is the average rate of growth observed between film rupture events. Asserting, as in development of Eqn. 1, that film rupture occurs when the accumulated creep strain exceeds the fracture strain of the oxide:

$$V_{scc} = \frac{M}{Z\rho F}\frac{Q}{t_r} = \frac{k_p}{\rho}\cdot\left(\frac{\dot{\varepsilon}_c}{\varepsilon_f}\right)^{1/2} \qquad \text{Eqn (7)}$$

This expression allows a direct comparison of alloys with different properties of corrosion kinetics, creep and rupture strain. To compare predicted SCC growth rates,

$$\frac{V_{16}}{V_{30}} = \frac{K_{p\text{-}16}}{K_{p\text{-}30}}\left[\frac{\dot{\varepsilon}_{c\text{-}16}}{\dot{\varepsilon}_{c\text{-}30}}\frac{\varepsilon_{f\text{-}30}}{\varepsilon_{f\text{-}16}}\right]^{1/2} \qquad \text{Eqn (8)}$$

where, $K_{p\text{-}16}$, $K_{p\text{-}30}$ - parabolic growth rate constants for 16% and 30% Cr alloys.

Both the kinetic and creep terms are temperature dependent, and the creep term is strongly stress dependent. The combined influence of the three parameters can be evaluated parametrically. For example, Fig. 12 shows how the SCC growth rate ratio of Eqn. 8 is predicted

to vary with temperature at high stress. For conditions of practical interest, such as at a common test temperature of 360° C and a highly stressed sample at applied stress to yield strength ratio of 2 or more, a difference in crack growth rate of about 10x is predicted. This would predict an average crack growth rate on the order of 10^{-11} to 10^{-12} m/s at this temperature for Alloy 690, if typically reported Alloy 600 growth numbers (35, 36) are used as the baseline. Available data indicates this overpredicts observed SCC growth rates in Alloy 690 (35). Crack growth rates of this magnitude have been demonstrated to be measurable (35). However, values on this order have not been reported in years of effort on Alloy 690. Therefore, the difference in crack growth rate predicted by applying the measured properties of creep rate, oxide rupture strain and corrosion kinetics underestimates the true effect of Cr. This analysis demonstrates that either the effect of Cr is dominant at the initiation phase or this formulation of the anodic dissolution model cannot fully account for the influence of Cr on SCC.

Conclusions

Corrosion kinetics of the alloy system were characterized gravimetrically, by exposing samples of the alloys to pure 288-360° C water. Corrosion kinetics display classic parabolic behavior. The corrosion rate of the alloys is measurably influenced by chromium concentration, with the parabolic constant first increasing with Cr concentration between 5 and 16%, then decreasing with increasing Cr.

The key material properties that influence the rate of SCC under an anodic dissolution process are oxide rupture strain, dissolution and repassivation kinetics, and base metal creep strength. Chromium concentration influences each of these properties in a manner that would decrease the predicted SCC rate, indicating that the anodic dissolution model is qualitatively consistent with the observed effect of Cr on SCC. When the materials properties measured in this study are combined with existing data and factored into the anodic dissolution model for SCC, the model predicts the effect of Cr on SCC growth rate to be smaller than observed in practice. This could be because Cr has a predominant effect on the SCC initiation process, or because some element of the mechanism by which Cr influences SCC growth rate is not accounted for in the anodic dissolution model as formulated here.

Acknowledgement

The assistance of Dr. J. Fish both in the experimental and analytical aspects of the program, is gratefully acknowledged.

References

1. Shack, W.J., "An Overview of Environmental Degradation of Materials in Nuclear Power Plant Piping Systems" (1988) Environmental Degradation of Materials in Nuclear Power Systems, Theus, G.J and Weeks, J.R, eds. The Metallurgical Society

2. Nagamo, H. and Kajumura, H. "Clarification of SCC Mechanism on Ni Base Alloys in Steam Generators for Their Long Term Assurance" (1995) Proceedings of the Seventh International Symposium on Env. Degradation of Materials in Nuclear Power Systems. NACE.

3. Sui, G., Titchmarsh, J.M., Heys, G.B. and Congleton, J., "Stress Corrosion Cracking of Alloy 600 and Alloy 690 in Hydrogen/Steam at 380 C", Corrosion Science, 39, No. 3 (1997), 565-587

4. Lowenstein, D.B, Shoemaker, C.E and Gorman, J.A. (1993) "Etching Techniques and Carbon Analysis for Alloy 690". Int. Symp. on Env. Degradation of Materials in Nuclear Power Systems. NACE.

5. Bursle, A.J. and Pugh, E.N. (1979) "An Evaluation of Current Models for the Propagation of Stress Corrosion Cracks", in Proceedings of Environment Sensitive Fracture of Engineering Materials, AIME, p. 18.

6. Craig, B., "Environmentally Assisted Cracking" (1987) Metals Handbook, Ninth Edition, v. 13, p. 145, American Society for Metals

7. Andresen, P.L. (1991) "Fracture Mechanics Data and Modeling of Environmental Cracking of Nickel-Base Alloys in High Temperature Water" Corrosion, 47(12) p.917

8. Shen, Y. and Shewmon, P.G. (1991) "IGSCC Crack Growth of Alloy 600 and X750 in Steam". Corrosion, 47 (9)

9. Anzai, H., Kuniya, J. and Masaoka, I. " A Methodology for Quantitative Evaluation of Hydrogen Assisted Cracking as One Mechanism of Environmental Assisted Cracking in High Temperature Pure Water", Proceedings of International Symposium on Plant Aging and Life Predictions of Corrodible Structures, (1995) Sapporo, Japan

10. Hall, M.M., "Thermally Activated Dislocation Creep Model for Primary Water Stress Corrosion Cracking of NiCrFe Alloys". NUREG/CP-0151(1996)

11. Ford, F.P and Andresen, P.L. "Development and Use of a Predictive Model of Crack Propagation in 304/316L,A533B/A508, and Inconel 600/182 Alloys in 288 C Water" (1988)

Environmental Degradation of Materials in Nuclear Power Systems, Theus, G.J and Weeks, J.R, eds. The Metallurgical Society

12. Andresen, P.L. "Modeling of Water and Material Chemistry Effects on Crack Tip Chemistry and Resulting Crack Growth Kinetics" (1988) Environmental Degradation of Materials in Nuclear Power Systems, Theus, G.J and Weeks, J.R, eds. The Metallurgical Society

13. Thompson, C.D,Lewis, N., Krasodomski, H.T. and Makar, G.L, (1995) "Prediction of PWSCC in Nickel Base Alloys Using Crack Growth Rate Models" Seventh International Symp. on Env. Degradation of Materials in Nuclear Power Systems. NACE.

14. Krasodomski,H.T.,Fish,J.S and Lewis,N.,"Analysis of PWSCC Initiation and Crack Growth in Laboratory Specimens and Components as a Function of Material Condition" ,EPRI Workshop on PWSCC if Alloy 600 in PWRs (1997)

15. Rosecrans, P.M. and Duquette, D. J., "Formation Kinetics and Rupture Strain of Ni-Cr-Fe Alloy Corrosion Films Formed in High Temperature Water", Metallurgical and Materials Transactions, to be published

16. Airey, G.P. (1980) "Microstructural Aspects of the Thermal Treatment of Inconel Alloy 600". Metallography, 13,p. 21

17. Alloy Digest. Engineering Alloys Digest (1972)

18. Ziemniak,S.E.,"Metal Oxide Solubility Behavior in High Temperature Aqueous Systems"J. Solution Chem.,21,8(1992) 745-760

19.Wagner,C.,"Theoretical Analysis of the Diffusion Processes Determining the Oxidation Rate of Alloys",J.Electrochem. Soc.,99(1952)369-380

20.Chattopadhyay,B. and Wood, G.B., "The Transient Oxidation of Fe-Cr and Ni-Cr Alloys",J. Electrochem. Soc., 117(1970)1163-1171

21.McIntyre, NS,Zetarink, DG, and Owen, D, "XPS Study of the Initial Growth of Oxide Films on Inconel 600 Alloy". Appl. Surf. 2(1978) 55-73

22.McIntyre, NS and Zetarink, DG "Quantitative analysis of Thin Oxide Films using X-ray Photoelectron spectroscopy and Rastered Ion Bombardment" J Vac Sci Tech. v14, 1/2/77

23. McIntyre, NS, Zetarink, DG, and Owen, D., "X-ray Photoelectron Studies of the Aqueous Oxidation of Inconel-600 Alloy", J. Electrochem. Soc., 126 (1979)750-760

24. Yamanaka, K. and Murayama, J. "Relationship Between Straining Electrode Behavior and Corrosion Film of Nickel Base Alloys in a High Temperature Caustic Solution" (1990) The Sumitomo Search, v. 142, p. 17

25.Copson, H.R. and Berry, W.E., "Corrosion of Inconel Nickel-Chromium Alloy in Primary Coolants of Pressurized Water Reactors", Corrosion, 18(1962)121-24.

26.Copson, H.R. and Berry, W.E., "Qualification of Inconel for Nuclear Power Plant Applications", Corrosion, 16(1960)79-85

27. Robertson, J. "The Mechanism of High Temperature Aqueous Corrosion of Stainless Steels". Corrosion Science, 1,31 (1991) 443-465

28. Giggens, C..S. and Petit, F.S., "Oxidation of Ni-Cr Alloys Between 800 and 1200 C" Trans. AIME 245,2495,2509 (1971)

29. Birks, N. and Meier, G.H., Introduction to High Temperature Oxidation of Metals. Edward Arnold Ltd, London (1983)

30. Angelieu, T.M., Paraventi, D. J. and Was, G.S. " The Creep and Intergranular Cracking of Ni-Cr-Fe-C in 360 C Water". Corrosion 95, Paper 186

31. Noel, D.,deBouvier, O.,Foct, F.,Mithieux, J. D. and Vaillant, F.,"Study of the Mechanisms of Stress Corrosion Cracking of Alloy 600 and Alloy 690 in Primary Water Reactor Conditions", Eurocorr '96

32. Hertzberg, J. and Was, G. S., " The Effect of Carbon Distribution on Deformation and Cracking of Ni-16Cr-9Fe-C Alloys" Proc. of Sixth Int. Symp. on Env. Degradation of Materials in Nuclear Power Systems.(1995) NACE.

33. Angelieu, T.M. and Was, G.S. (1994) "Creep and Intergranular Cracking of Ni-Cr-Fe-C in 360 C Argon". Met. and Mat. Trans. A, 25A, p.1169

34. Mithieux,J-D.,Vaillant,F.,Buisine,D.,Brechet,Y. and Louchet,F.,"Influence of Chromium Content on Passivity and Creep Behavior of Nickel Base Alloys in Primary Water", Eurocorr '96

35. Sui, G., Titchmarsh, J.M., Heys, G.B. and Congleton, J., "Stress Corrosion Cracking of Alloy 600 and Alloy 690 in Hydrogen/Steam at 380 C", Corrosion Science,39,No. 3 (1997),565-587

36. Foster, J.P, Bamford, W.H. and Pathania, R.S.,"Initial Results of Alloy 600 Crack Growth Rate Testing in a PWR Environment". Seventh International Symp. on Env. Degradation of Materials in Nuclear Power Systems. NACE. (1995)

Table 1 Composition of NiFeCr Alloys (wt%)

Alloy	ID	Ni	Fe	Cr	C	Al	Ti	Mn	σ_y (ksi)
Low Cr	D06	85.6	8.0	4.6	0.030	0.11	0.24	0.44	34.9
Alloy 600[1]	DP1	74.0	8.5	15.9	0.080	0.14	0.23	0.34	45.8
Med Cr	D07	67.4	7.8	23.0	0.037	0.06	0.25	0.47	47.8
Alloy 690	D08	60.0	8.2	30.0	0.050	0.04	0.25	0.52	62.8
Alloy 690[1]	DP2	59.8	8.3	29.5	0.026	0.31	0.32	0.29	48.9
High Cr	D09	50.3	8.6	39.2	0.053	0.01	0.22	0.53	69.9

Notes: 1) commercial alloys: Alloy 690-Teledyne heat 9486, Alloy 600 Huntington heat NX2922G.

2) room temperature yield strength (0.2% offset method)

TABLE 2

Summary of Oxide Film AEM Observations

Sample ID	% Cr	Exposure Days	Phases Present				Oxide Grain Size (nm)		Other
			NiOOH	NiO	Spinels	Chromia	Inner	outer	
			Short Exposure Films						
DO6003	5	5		X	Trace		10	NA	1
DO6019	5	5	Trace	X			5-10	100	1
DO7017	23	5		X			5	100	2
DO9021	39	5		X	X		5		1
			Long Exposure Films						
DO6016	5	91		X			10	200	1
PHT-254	16	1095			X	X	10-20	200	1
DO7004	23	64			X		2	200	1
DO7013	23	64		X		Trace	5-10	150	1
DP2025	30	64		X	X		10-20	100	3,4
DP2004	30	64			X	Trace	5-15	100	2
DO9007	39	64			X	Trace	10-20	300	1,4
DO9001	39	64			X		5		1

Notes:

1. Spatial Cr and/or Fe variability
2. Isolated Elongated Oxide Grains
3. High Volume Fraction of Fine Oxide
4. Locally Coarse Outer film (>1000 nm)

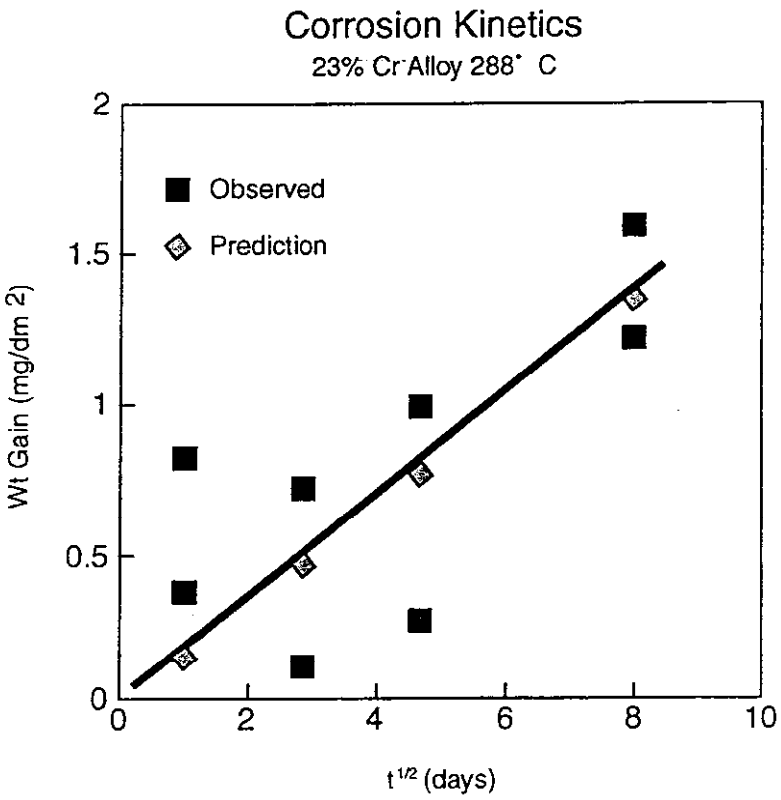

Figure 1. General corrosion kinetics for 23% Cr alloy.

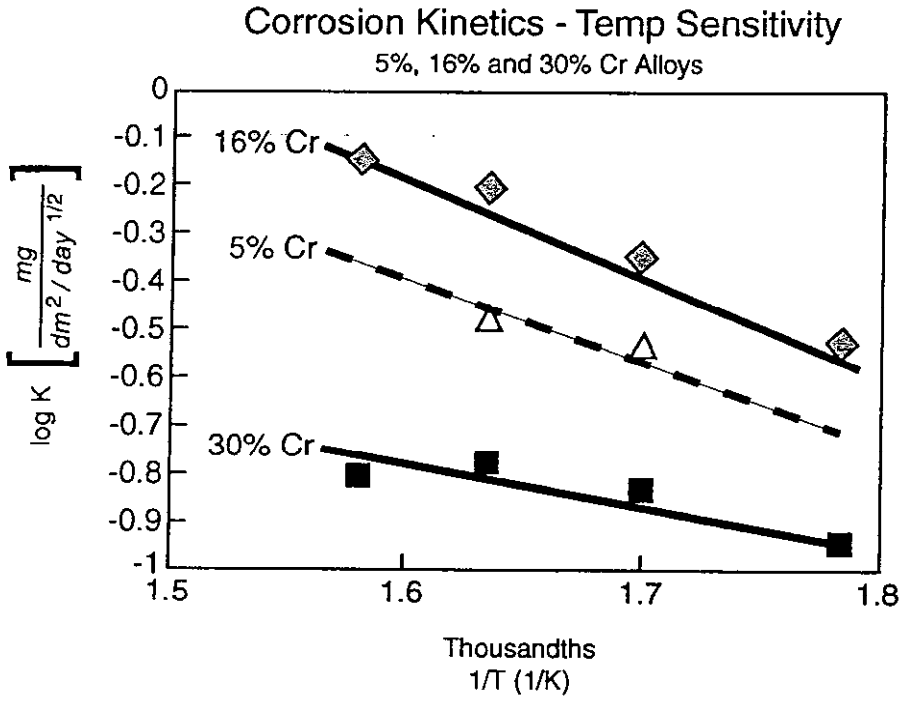

Figure 2. Effect of Temperature on Parabolic Constant for Alloys with Different Cr Content

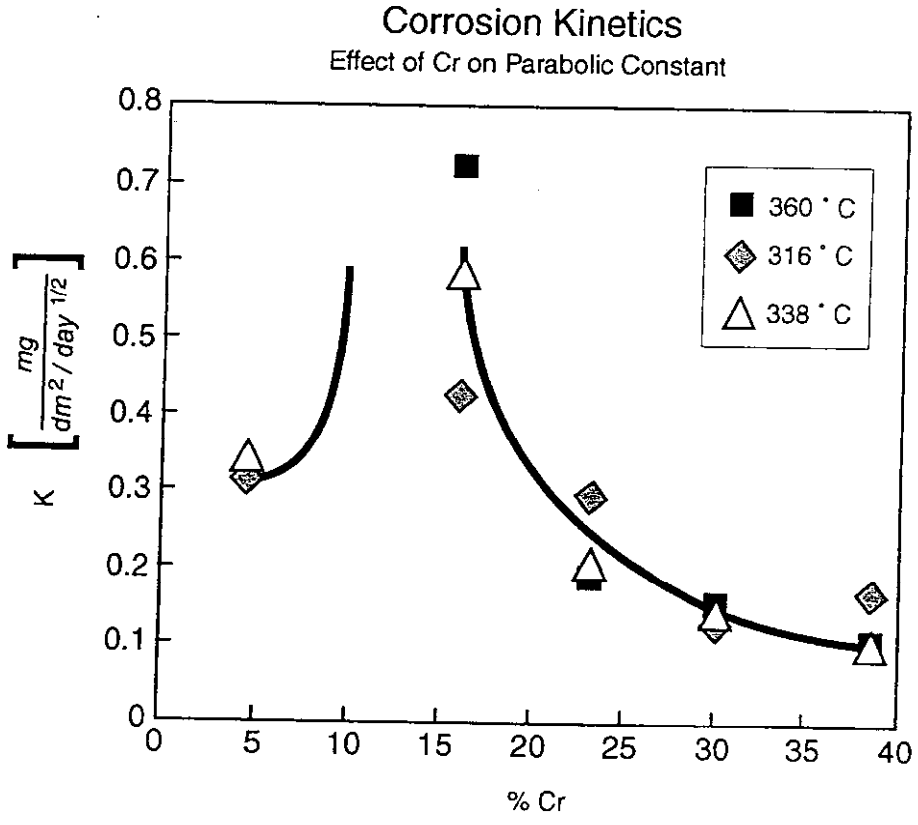

Figure 3. Effect of Chromium on Parabolic Rate Constant.

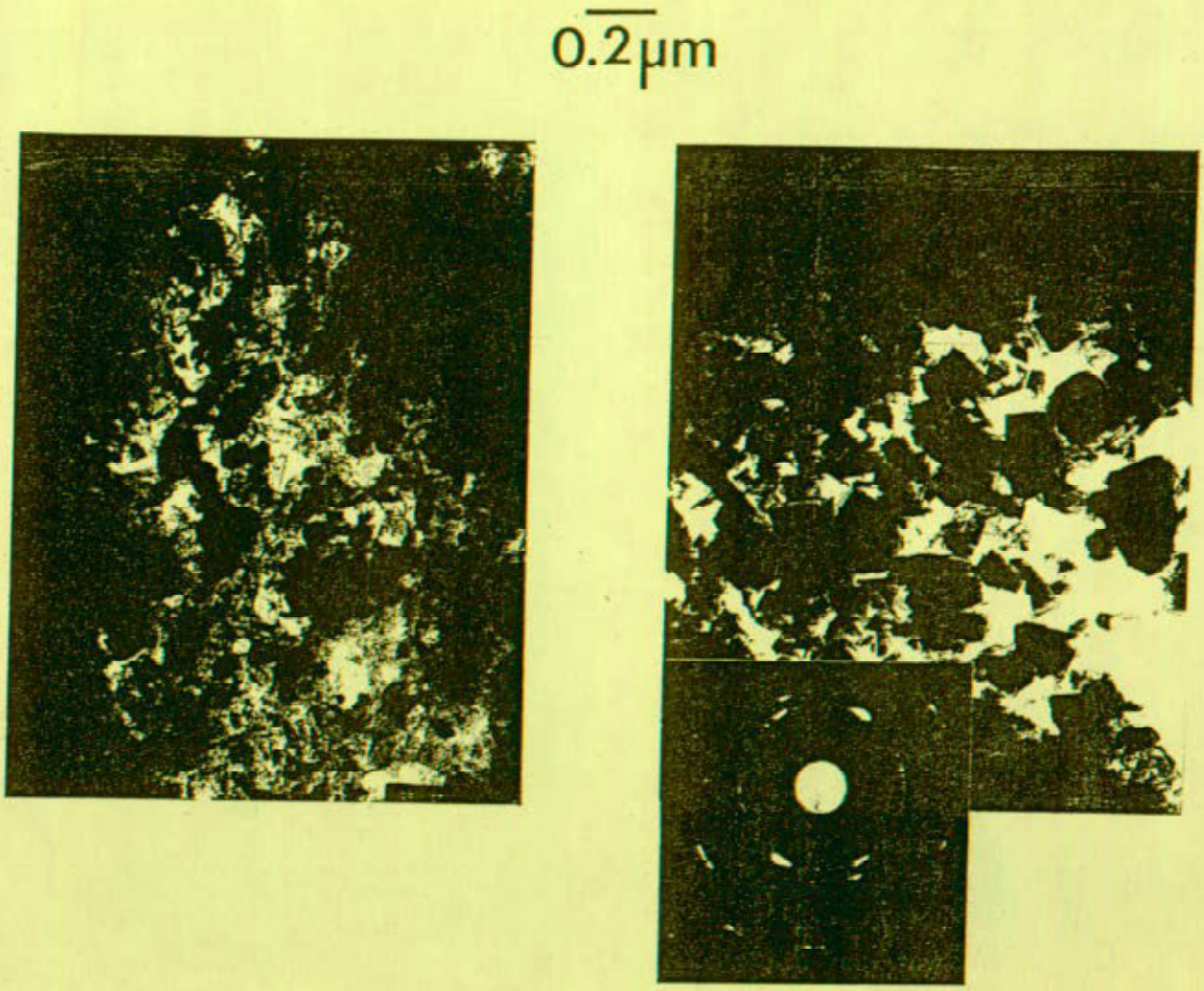

Figure 4 Bright Field AEM Images from sample with 23% Cr, exposed to 288°C water for 5 days. Gradation in grain size is evident, with the finest grains at the metal-oxide interface. Diffraction patterns index to NiO.

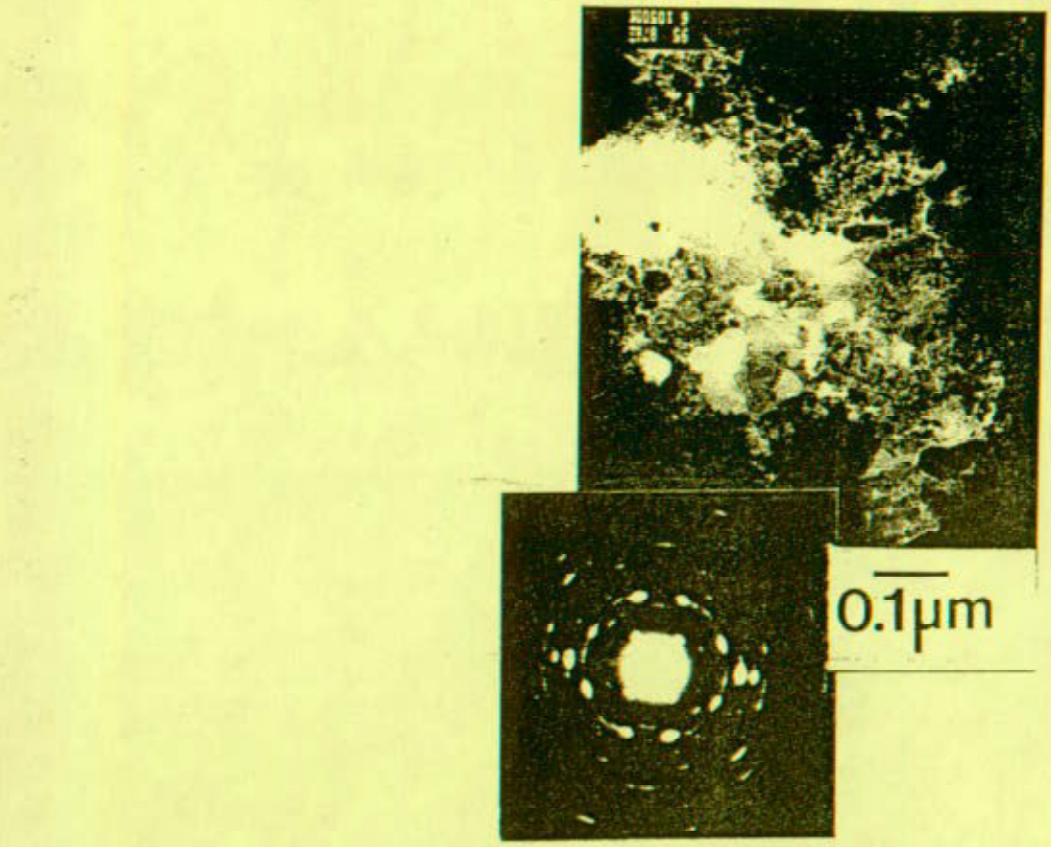

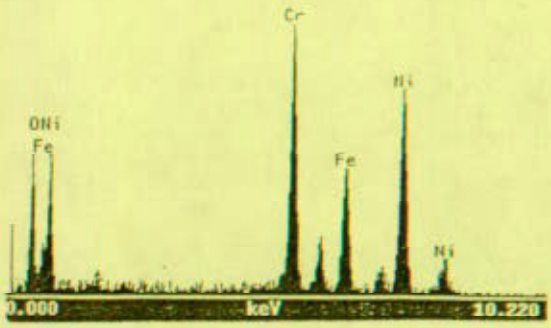

inner film spectra

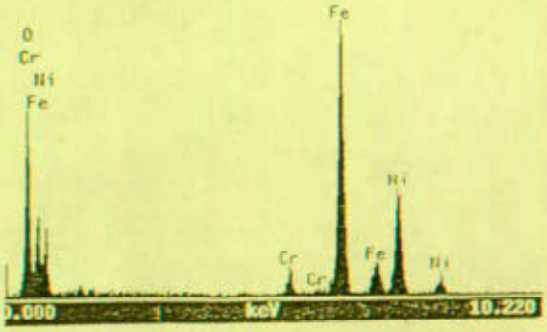

outer film spectra

Figure 5 Bright Field AEM Images and Analysis Spectra from sample with 23% Cr exposed to 360°C water for 64 days. Grain size gradation is evident. Spinel diffraction patterns predominate, with a mix of cubic (NiO) and hexagonal (Cr_2O_3) spots.

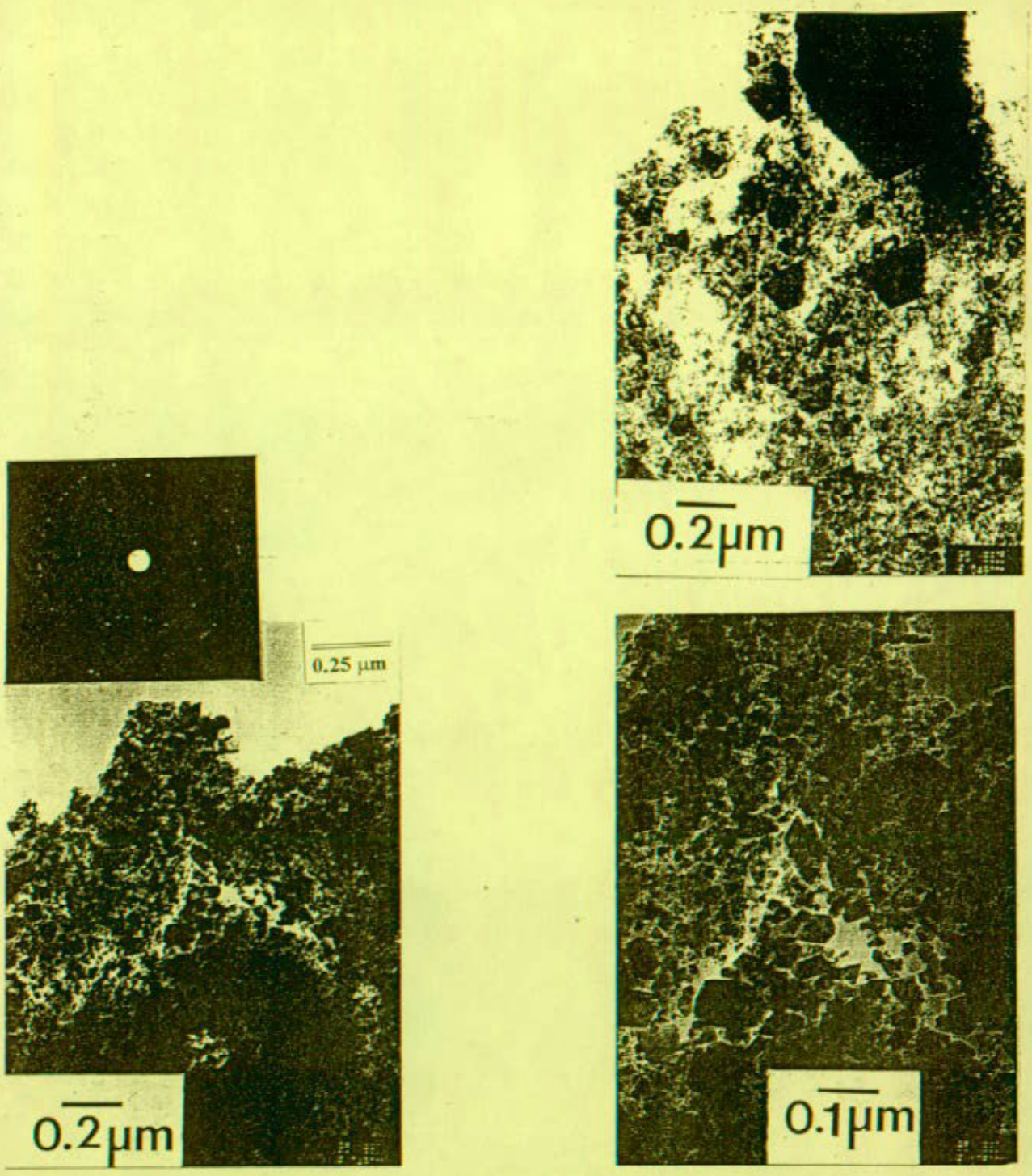

Figure 6 Images from sample of 39% Cr alloy exposed to 360°C water for 64 days. Grain size gradation, including blocky outer $NiFe_2O_4$, is evident. Spinel diffraction patterns dominate, with some hexagonal phase.

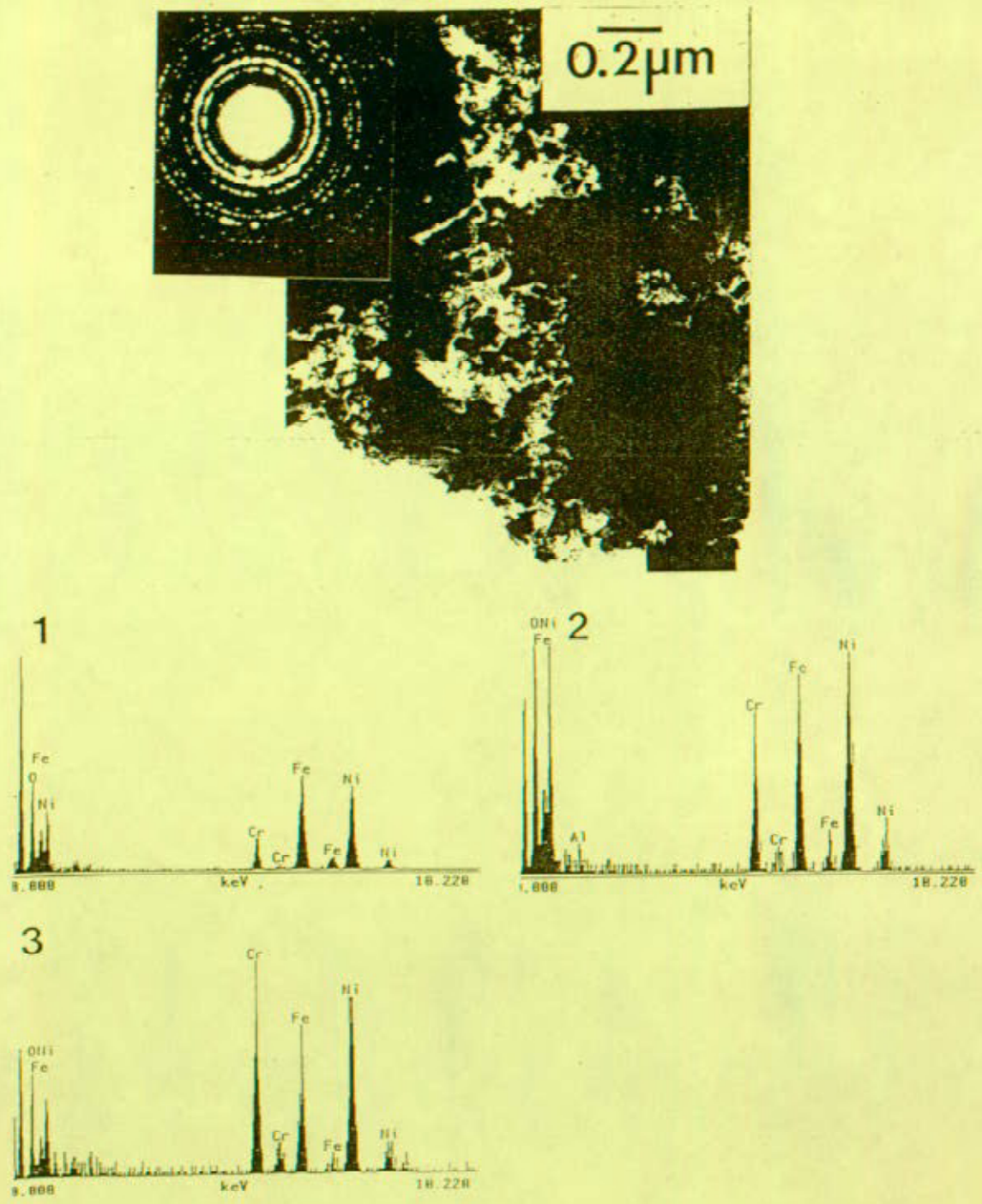

Figure 7 Outer oxide microstructure for sample exposed to 288°C water for 1095 days. Electron diffraction shows a spinel pattern, composition ranges locally from Fe rich to Cr rich.

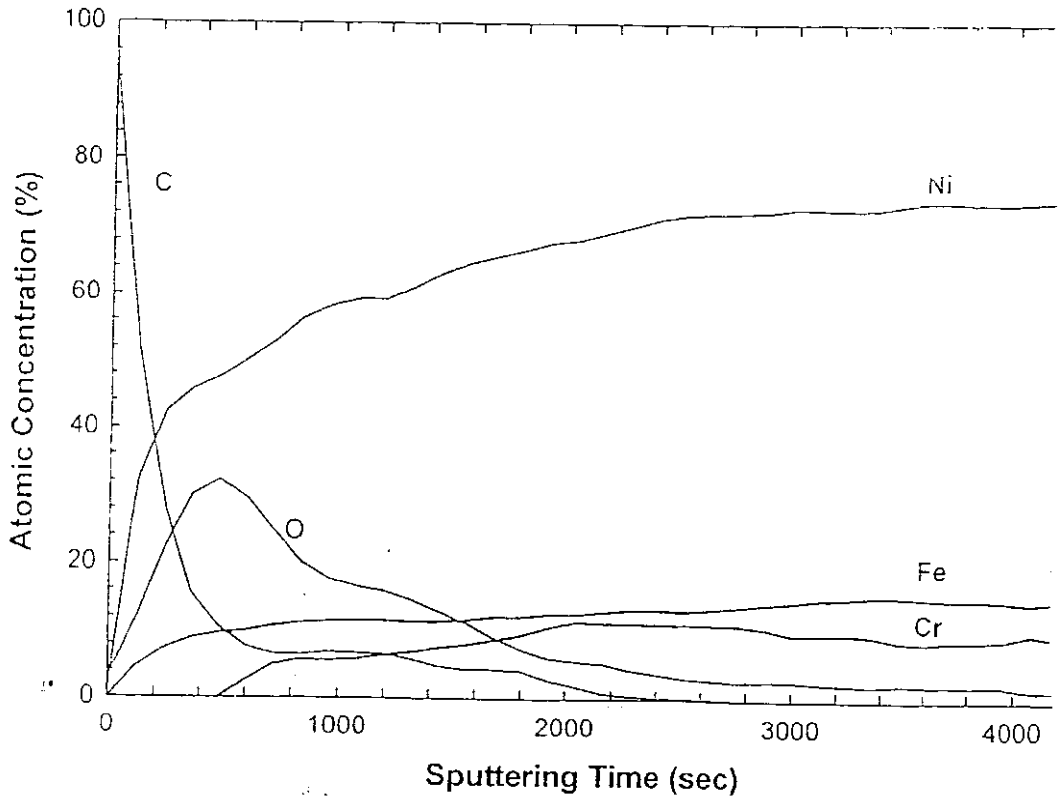

Figure 8 AES composition depth profile for the 5% Cr alloy. Both Fe and Cr concentration decrease with distance from the metal oxide interface.

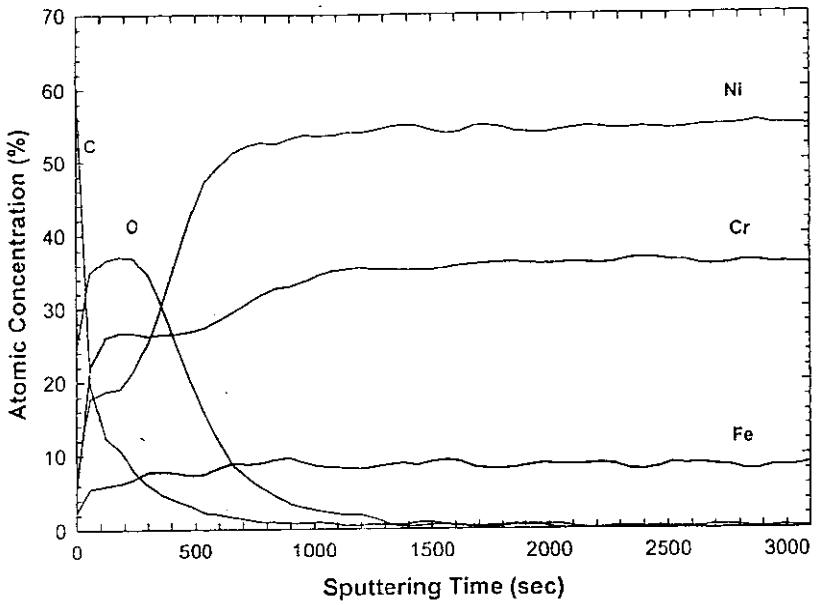

Figure 9 AES composition depth profiles for Alloy 690. Cr concentration drops off abruptly with distance from the metal oxide interface, while Fe concentrations drops more gradually.

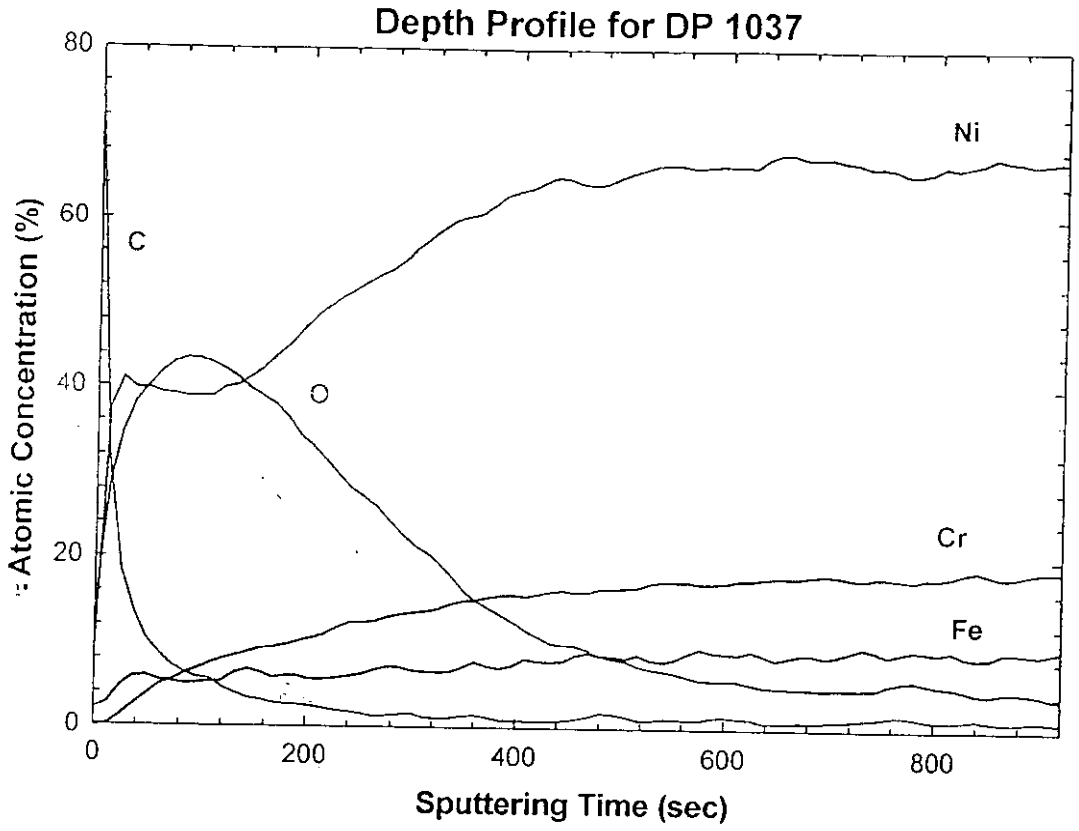

Figure 10 AES composition depth profile for Alloy 600. Both Fe and Cr concentration decrease with the distance from the metal oxide interface.

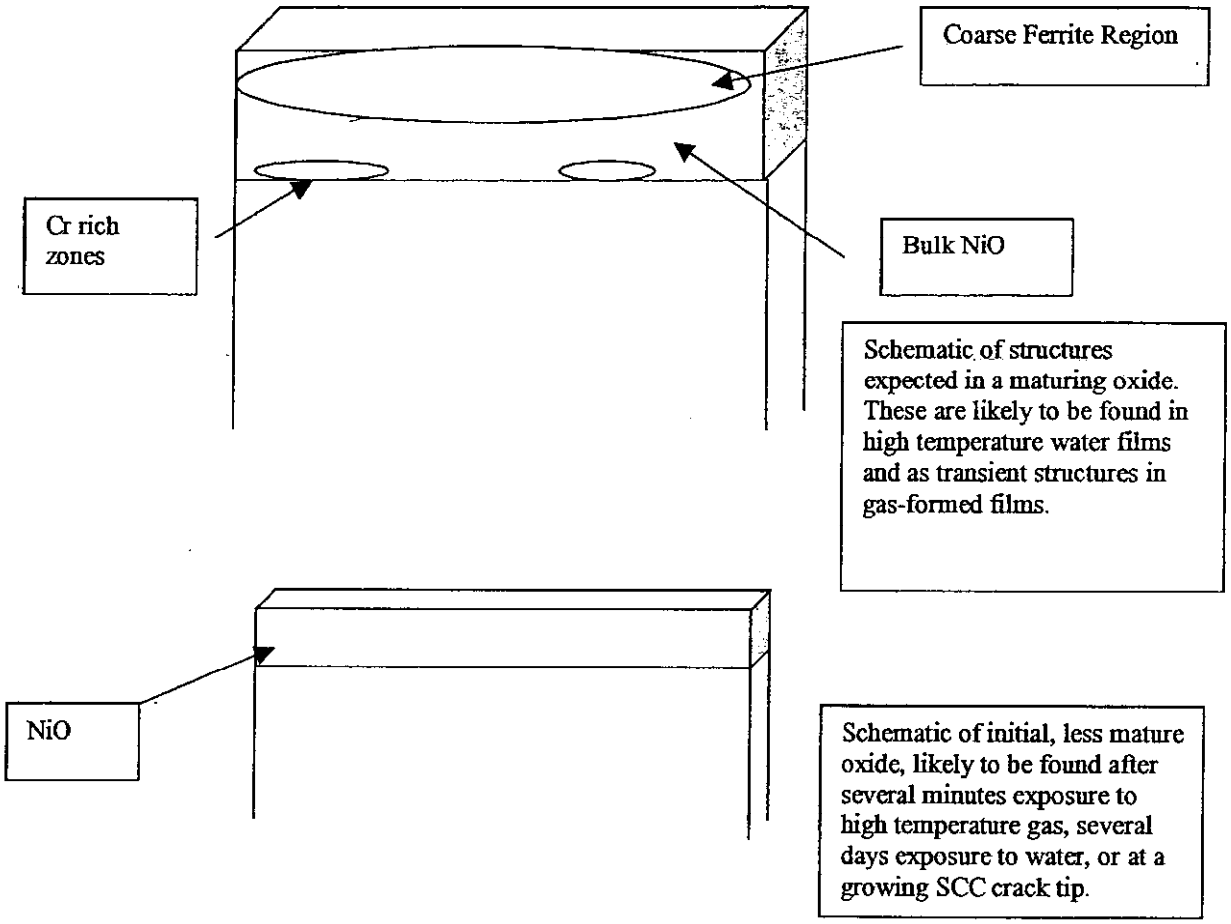

Figure 11 Schematics of Oxide Film Formation Process for NiFeCr Alloys in High Temperature Water

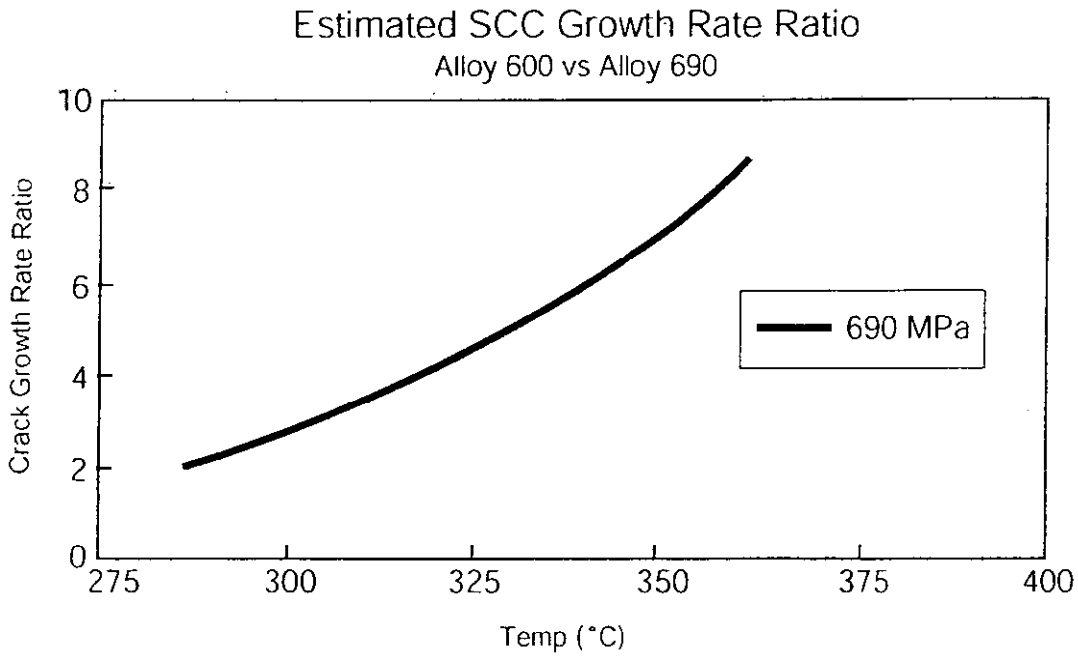

Anodic Dissolution Model with Material Property Inputs

Figure 12 Predicted SCC Growth Rate Comparison for 16% and 30% Cr alloys. Anodic Dissolution model assumptions of Equation 8 apply